THE JOURNAL OF PHYSICAL CHEMISTRY LETTERS
A JOURNAL OF THE AMERICAN CHEMICAL SOCIETY

pubs.acs.org/JPCL

Letter

Reversible Zinc Electrodeposition at −60 °C Using a Deep Eutectic Electrolyte for Low-Temperature Zinc Metal Batteries

Brendan E. Hawkins, Theresa Schoetz, Leo W. Gordon, Surabh KT, Jonah Wang, and Robert J. Messinger*

Cite This: *J. Phys. Chem. Lett.* 2023, 14, 2378−2386

Read Online

ACCESS | Metrics & More | Article Recommendations | Supporting Information

ABSTRACT: Rechargeable zinc (Zn) metal batteries are attractive for use as electrochemical energy storage systems on a global scale because of the low cost, high energy density, inherent safety, and strategic resource security of Zn metal. However, at low temperatures, Zn batteries typically suffer from high electrolyte viscosity and unfavorable ion transport properties. Here, we studied reversible Zn electrodeposition in mixtures of 1-ethyl-3-methyl-imidazolium bis(trifluoromethylsulfonyl)imide ([EMIm]TFSI) ionic liquid, γ-butyrolactone (GBL) organic solvent, and $Zn(TFSI)_2$ zinc salt. The electrolyte mixtures enabled reversible Zn electrodeposition at temperatures as low as −60 °C. An electrolyte composed of 0.1 M $Zn(TFSI)_2$ in [EMIm]TFSI:GBL with a volume ratio of 1:3 formed a deep eutectic solvent that optimized electrolyte conductivity, viscosity, and the zinc diffusion coefficient. Liquid-state ^1H and ^{13}C nuclear magnetic resonance (NMR) spectroscopy and molecular dynamic (MD) simulations indicate increased formation of contact ion pairs and the reduction of ion aggregates are responsible for the optimal composition.

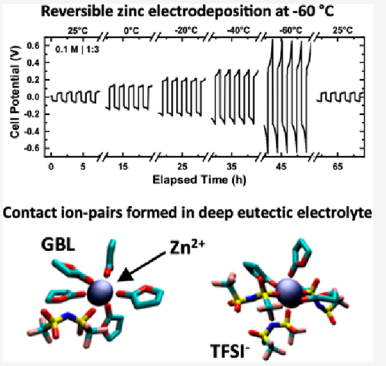

As low-cost rechargeable batteries have become more widespread over the past decade, the market for battery-powered devices, equipment, and vehicles has grown significantly. There now exists a demand for batteries that function in low-temperature environments such as high altitude, cold climates, or outer space. However, most rechargeable batteries are limited to operation at moderate temperatures. Although heaters are commonly employed to maintain a suitable operating temperature in cold environments, they add mass, volume, and system complexity while reducing overall gravimetric and volumetric energy density. Thus, there is a need for batteries that can function at low temperatures without thermal management.[1]

The lower operating temperature for batteries is often limited by the freezing point of the electrolyte or by slow ion transport. Methods in lithium-ion battery research for lowering electrolyte operating temperature include combining dissimilar organic solvents to improve ion transport[2] and lowering the solvent freezing point.[3] These methods have been successful in enabling moderate low-temperature operation of lithium-ion batteries for commercial use; however, the recommended operating temperature is typically limited to −20 °C[4,5] because the energy delivered at low temperature is drastically reduced.[6] For many applications, this limit is restrictive. For example, widespread, reliable use of electric vehicles requires operation at −30 °C,[6] and many defense and space applications require operation at −50 °C and below.[1,7] Thus, low-temperature performance must be improved to enable new applications for rechargeable batteries.

One strategy to enable battery operation at low temperatures is to use ionic liquids (IL) or deep eutectic solvents (i.e., liquid mixtures at or near their eutectic point[8]) that have wide liquid temperature windows, remaining liquid below −100 °C in some cases.[9,10] The broad operating temperature ranges afforded by this wide liquid window are attractive for use in extreme environments, such as in aerospace applications. ILs are also attractive for their high electrochemical stability windows, which enable operation at high potentials, and nonflammability, which improves safety.[11] Alternative battery chemistries to lithium-ion batteries are being considered for low temperature applications. Batteries using zinc metal (Zn) have been the subject of recent studies[12,13] in part because of the low cost, high energy density, low toxicity, inherent safety, and strategic resource security of Zn metal. Zn has historically been used in single-discharge alkaline batteries for over a century, and more recently, there has been growing interest in developing rechargeable Zn batteries for applications such as grid storage, renewable energy storage, and electrified transportation.[14−16]

Ionic liquid electrolytes have been a growing subject of research for improving the reversibility of Zn electroplating

Received: January 16, 2023
Accepted: February 20, 2023
Published: February 27, 2023

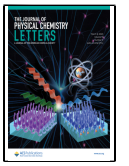

https://doi.org/10.1021/acs.jpclett.3c00150
J. Phys. Chem. Lett. 2023, 14, 2378−2386

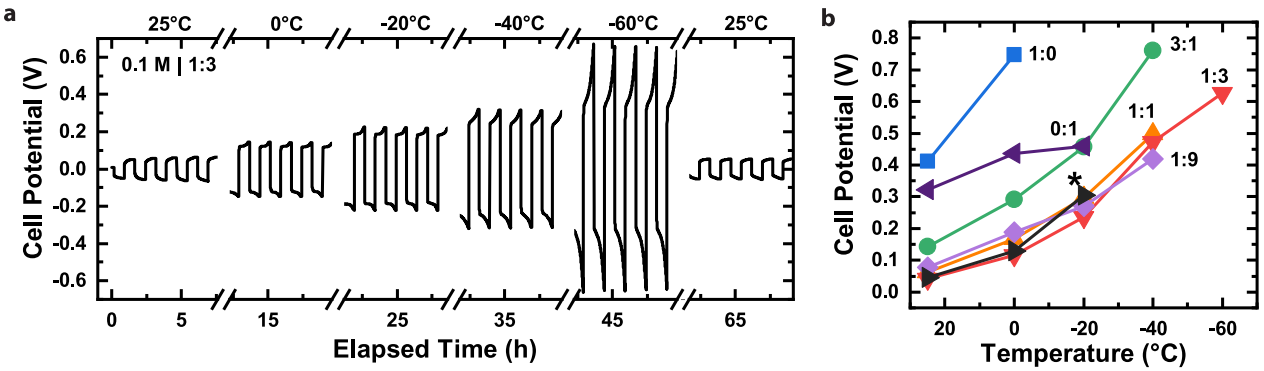

Figure 1. (a) Variable-temperature galvanostatic cycling of symmetric Zn-Zn two-electrode cells at 0.01 mA cm^{-2} using 0.1 M $Zn(TFSI)_2$ in [EMIm]TFSI:GBL (1:3 vol. ratio). (b) Maximum recorded potentials at temperatures of 25, 0, −20, −40, and −60 °C using 0.1 M $Zn(TFSI)_2$ in [EMIm]TFSI:GBL with volume ratios of 0:1, 1:9, 1:3, 1:1, 3:1, and 1:0 (indicated on plot) as well as 1.0 M $Zn(TFSI)_2$ in [EMIm]TFSI:GBL with a volume ratio of 1:1 (indicated by *). Mixing the [EMIm]TFSI and GBL lowered the overpotential up to a factor of ∼10.

and stripping by eliminating the hydrogen evolution reaction (HER) that occurs at the Zn metal electrode in aqueous electrolyte. Recently, a 1-ethyl-3-methyl-imidazolium (EMIm) tetrafluoroborate ionic liquid electrolyte was shown to suppress hydrogen generation and dendrite growth, improving Zn electrode performance.[17] Additionally, in a deep eutectic solvent of acetamide and zinc bis(trifluoromethylsulfonyl)-imide (TFSI), the $TFSI^-$ anion was shown to decompose, forming a solid electrolyte interphase that enables reversible Zn electroplating.[18] Other mixed-solvent systems have also shown promise for enabling low-temperature Zn batteries.[19] Despite these advantages, ionic liquids can have low specific ionic conductivities compared to aqueous electrolytes, often resulting from high viscosity at low temperatures[20] or high Zn salt concentrations.[21] One strategy to decrease viscosity and improve ion mobility is to mix the ionic liquid with an organic solvent, such as γ-butyrolactone (GBL), as demonstrated for low-temperature supercapacitors.[22] Separately, GBL has also been shown to enable the reversible electrodeposition of aluminum due to its ability to coordinate with multivalent cations.[23]

Here, we show that electrolyte mixtures composed of [EMIm]TFSI ionic liquid, GBL organic solvent, and $Zn(TFSI)_2$ zinc salt exhibit improved Zn electroplating and stripping at low temperatures compared to single-solvent electrolytes. An electrolyte composed of 0.1 M $Zn(TFSI)_2$ in [EMIm]TFSI:GBL with a volume ratio of 1:3 formed a deep eutectic solvent with the greatest specific conductivity, highest Zn diffusivity, and lowest viscosity, which enabled reversible Zn electroplating and stripping at temperatures as low as −60 °C.

Electrolyte composition was varied, specifically the [EMIm]-TFSI, GBL, and $Zn(TFSI)_2$ content, and the resulting electrolyte mixtures were studied to examine if they exhibited improved abilities to reversibly electroplate and strip Zn metal at low temperatures compared to single-solvent electrolytes. Galvanostatic cycling experiments were performed on symmetric Zn-Zn two-electrode cells at temperatures between 25 and −60 °C using electrolyte formulations with varying [EMIm]TFSI:GBL volume ratios and $Zn(TFSI)_2$ concentrations. For example, a variable-temperature galvanostatic cycling experiment performed with an electrolyte composed of 0.1 M $Zn(TFSI)_2$ in [EMIm]TFSI:GBL with a volume ratio of 1:3 enables reversible Zn electroplating and stripping down to −60 °C (Figure 1a). For all experiments, the maximum potential recorded at each temperature was plotted to compare low-temperature performance between electrolyte formulations (Figure 1b). If a data point is not shown for an electrolyte at a given temperature, then its potential reached the cutoff potential of 1 V, and the experiment was stopped.

Comparing Zn electroplating and stripping in different electrolyte formulations reveals the benefits of mixing [EMIm]TFSI and GBL. At 25 °C and zinc salt concentrations of 0.1 M $Zn(TFSI)_2$, the total overpotential reached 0.41 or 0.32 V for the single-solvent electrolytes using [EMIm]TFSI ionic liquid or GBL organic solvent, respectively, but only 0.04 V for a mixture consisting of [EMIm]TFSI:GBL in a volume ratio of 1:3. Thus, the total overpotential was up to an order-of-magnitude lower when using the mixed-solvent electrolyte, compared to the single-solvent electrolytes. This ∼10× reduction in overpotential reveals a striking improvement in electrochemical performance upon mixing the two solvents. Further, the single-solvent electrolytes did not support Zn electroplating and stripping within the 1 V limit at temperatures below −20 °C, whereas the mixed-solvent electrolyte containing a 1:3 volume ratio of [EMIm]TFSI:GBL cycled reversibly down to −60 °C. Comparing different [EMIm]-TFSI:GBL solvent ratios, when the GBL content is increased to a volume ratio of 1:9, the electrolyte no longer supports facile reversible plating and stripping at −60 °C. Thus, there exists an optimal electrolyte composition near a 1:3 volume ratio of [EMIm]TFSI:GBL.

Comparing zinc salt concentrations of 0.1 and 1.0 M $Zn(TFSI)_2$ in [EMIm]TFSI:GBL with a 1:1 volume ratio reveals that a lower Zn salt concentration enables improved Zn electroplating and stripping at lower temperatures. The two electrolytes have similar overpotentials at 25, 0, and −20 °C; however, at −40 °C and below, the electrolyte with 1.0 M $Zn(TFSI)_2$ does not support electroplating and stripping within the 1 V limit, whereas the 0.1 M $Zn(TFSI)_2$ electrolyte does. This result indicates high salt concentration does not support facile electroplating and stripping at lower temperatures because of the electrolyte's significantly higher viscosity and lower specific conductivity, as shown below. Overall, a low concentration of $Zn(TFSI)_2$ is critical for enabling reversible plating and stripping at low temperatures down to −60 °C.

To further investigate the electrolyte properties influencing reversible Zn electrodeposition, galvanostatic electrochemical impedance spectroscopy (GEIS) and variable-rate cyclic voltammetry (CV) were performed on different electrolyte

https://doi.org/10.1021/acs.jpclett.3c00150
J. Phys. Chem. Lett. 2023, 14, 2378−2386

formulations containing 0.1 M $Zn(TFSI)_2$ at 25 °C to measure their specific conductivities and estimate zinc diffusion coefficients and electrolyte viscosities. GEIS data indicated that the specific conductivity exhibits a maximum, 142 mS cm^{-1}, at a [EMIm]TFSI:GBL volume ratio of 1:3 (Figure 2a). This specific conductivity was ~3× higher than those of the single-solvent electrolytes, which were 50 and 44 mS cm^{-1} for electrolytes with [EMIm]TFSI and GBL, respectively.

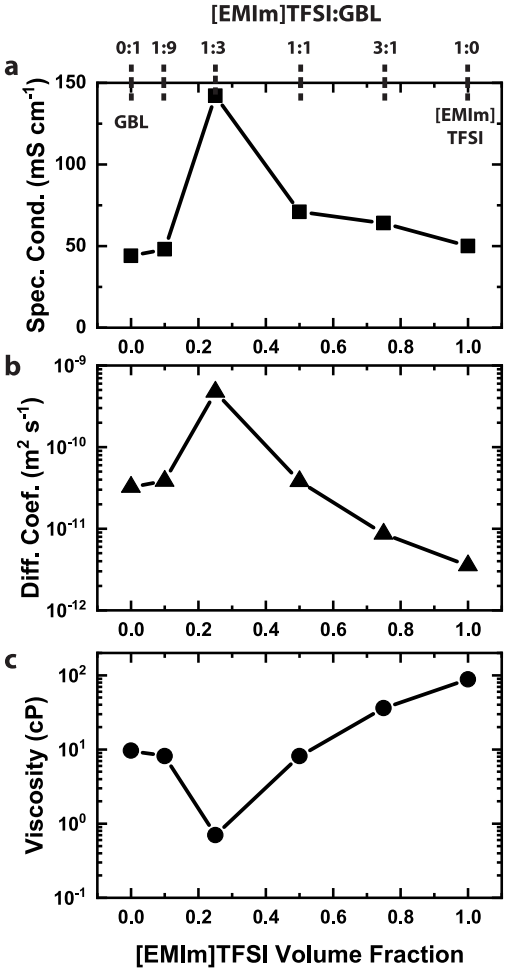

Figure 2. Electrolyte properties determined from electrochemical experiments at 25 °C: (a) specific conductivity, (b) zinc diffusion coefficient, and (c) viscosity of 0.1 M $Zn(TFSI)_2$ in [EMIm]-TFSI:GBL with volume ratios of 0:1, 1:9, 1:3, 1:1, 3:1, and 1:0 (denoted on top horizontal axis).

Zinc diffusion coefficients (Figure 2b) and electrolyte viscosities (Figure 2c) were calculated from variable-rate CV data (Figure 3) via the Randles-Ševčík (eq 1) and Stokes-Einstein (eq 2) relationships, respectively. The zinc diffusion coefficient is a weighted average of contributions from any solvated zinc species capable of electrodepositing to zinc metal at the electrode surface, the process which gives rise to the measured current on which the calculation is based. The different solvated zinc species are analyzed by liquid-state NMR measurements and MD simulations below. As a function of electrolyte composition, the zinc diffusion coefficient followed a similar trend to the specific conductivity and was also the greatest, 5×10^{-10} m^2 s^{-1}, for the electrolyte composed of 0.1 M $Zn(TFSI)_2$ in [EMIm]TFSI:GBL with a

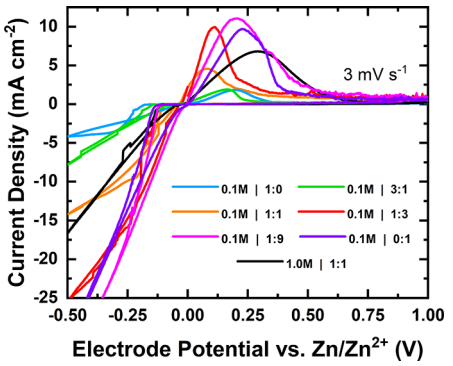

Figure 3. Cyclic voltammetry performed with glassy carbon rods and a Zn-wire quasi-reference electrode acquired at 3 mV s^{-1} and 25 °C using electrolytes composed of 0.1 M $Zn(TFSI)_2$ in [EMIm]-TFSI:GBL with volume ratios of 0:1, 1:9, 1:3, 1:1, 3:1, and 1:0 as well as 1.0 M $Zn(TFSI)_2$ in [EMIm]TFSI:GBL with a volume ratio of 1:1.

volume ratio of 1:3. This mixed-solvent electrolyte had a zinc diffusion coefficient ~100× higher or ~10× higher compared to the single-solvent electrolytes using [EMIm]TFSI or GBL, respectively.

The viscosity of the single-solvent electrolytes containing 0.1 M $Zn(TFSI)_2$ in either [EMIm]TFSI or GBL solvents was estimated to be approximately 100 or 10 cP, respectively. The viscosity was the lowest, 0.7 cP, for the electrolyte mixture with a 1:3 volume ratio of [EMIm]TFSI:GBL. Literature values for neat [EMIm]TFSI and GBL without added zinc salt are 35 and 2 cP, respectively, which are expected to increase with the addition of zinc salt. Thus, the viscosity estimates are reasonable and confirm the utility of the Stokes−Einstein equation even for nonideal solvents.

Additionally, the electrolyte composed of 1.0 M $Zn(TFSI)_2$ in 1:1 [EMIm]TFSI:GBL (data not shown) had a viscosity ~500× greater than that of the similar electrolyte containing 0.1 M $Zn(TFSI)_2$. The electrolyte with higher salt concentration also had a specific conductivity of 30 mS cm^{-1}, which is lower than all of the electrolyte formulations containing 0.1 M $Zn(TFSI)_2$. The increase in viscosity and reduction in specific conductivity upon salt addition explain why using lower concentrations of Zn salt in these mixed electrolyte systems resulted in lower overpotentials for reversible Zn electrodeposition at lower temperatures.

Differential scanning calorimetry (DSC) experiments establish that no thermodynamic phase transitions occur between 25 and −80 °C (lower temperature limit of the DSC equipment) in the electrolyte composed of 0.1 M $Zn(TFSI)_2$ in [EMIm]TFSI:GBL with a volume ratio of 1:3, confirming its melting point is below −80 °C (Table 1 and Figures S1, S2, S3, Supporting Information). Further, DSC measurements reveal freezing points of −20 and −54 °C for the single-solvent electrolytes composed of 0.1 M $Zn(TFSI)_2$

Table 1. Melting Points of Selected Electrolytes Measured by DSC[a]

electrolyte composition with 0.1 M $Zn(TFSI)_2$	melting point
[EMIm]TFSI	−20 °C
GBL	−54 °C
[EMIm]TFSI:GBL, vol. ratio 1:3	<−80 °C

[a]Note that the lower temperature limit of the DSC equipment was −80 °C.

https://doi.org/10.1021/acs.jpclett.3c00150
J. Phys. Chem. Lett. 2023, 14, 2378−2386

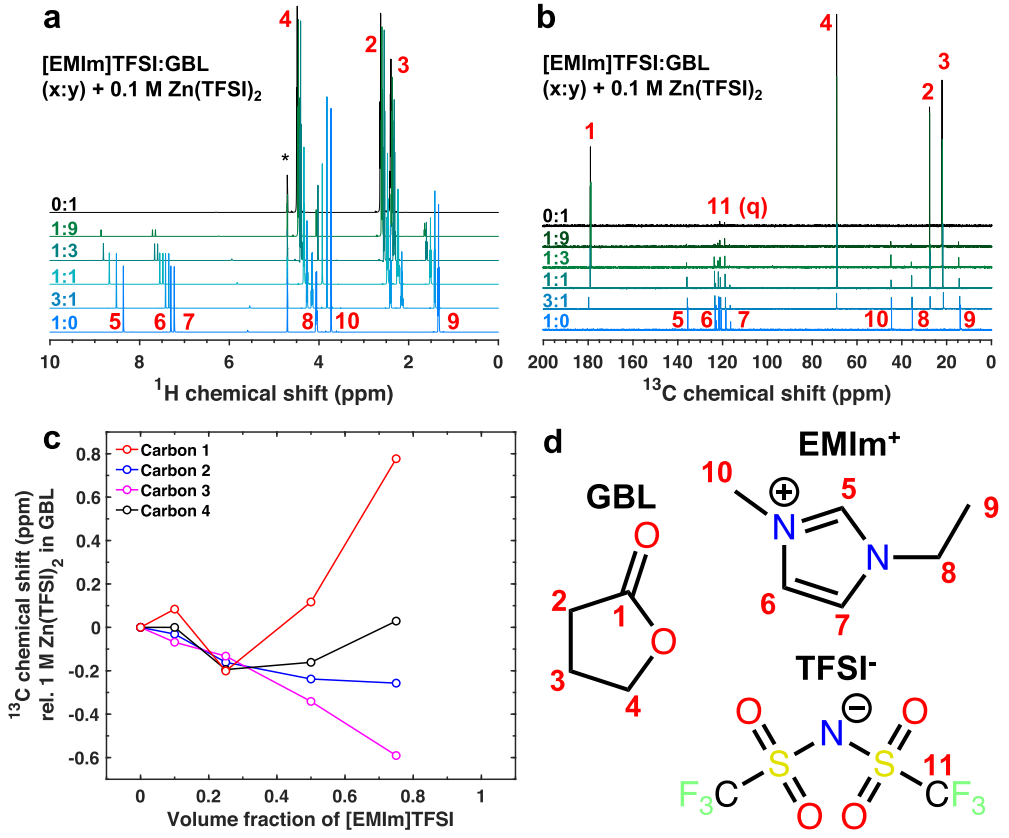

Figure 4. Liquid-state (a) ^{1}H and (b) ^{13}C single-pulse NMR spectra of 0.1 M $Zn(TFSI)_2$ in [EMIm]TFSI:GBL with volume ratios of 0:1, 1:9, 1:3, 1:1, 3:1, and 1:0. (c) Relative ^{13}C chemical shifts with respect to the single-solvent GBL electrolyte as a function of the [EMIm]TFSI volume fraction. (d) Molecular structures of GBL, $EMIm^+$, and $TFSI^-$ with numbers corresponding to the ^{1}H and ^{13}C chemical shift assignments in (a) and (b). Residual ^{1}H signals from D_2O, used as a locking solvent within a separate coaxial tube, are marked with * in (a).

in [EMIm]TFSI and GBL, respectively, slightly lower than literature values of −16 and −44 °C for the neat solvents without Zn salt, respectively, as expected. These results confirm that [EMIm]TFSI and GBL form eutectic mixtures, where the melting point of the mixture is lower than those of its individual components. Upon addition of 0.1 M $Zn(TFSI)_2$, the greatest specific conductivity, highest zinc diffusion coefficient, and minimum viscosity were all observed when using a mixture of [EMIm]TFSI:GBL in a volume ratio of 1:3. Thus, [EMIm]TFSI:GBL in a volume ratio of 1:3 may be near the eutectic point in the binary [EMIm]TFSI-GBL phase diagram; further study of this mixture without zinc salt would be interesting to determine if this is the case. Various definitions for deep eutectic solvents exist, the simplest being an electrolyte mixture at or near its eutectic point,[8] which we use here. Note that some restrict classification to mixtures whose melting point depression is greater than expected from ideal mixing.[24]

The reduced melting temperature upon mixing can be understood thermodynamically in terms of increasing the entropy of the liquid phase. Mixing two or more different components increases the entropy of the system, while choosing an asymmetric molecule such as the $EMIm^+$ cation can increase entropy further.[25,26] This increase in disorder inhibits the efficient ordering of molecules in the electrolyte, suppressing the melting point.[27,28] In turn, ion mobility is improved far from the melting point, resulting in the increased specific conductivity, lower viscosity, and a greater zinc diffusion coefficient. These effects impact the physicochemical properties of the electrolytes but do not fully explain the remarkable performance of the optimal electrolyte, which is influenced by the molecular-level solvation environments. To better understand the origin of the optimum electrolyte composition at molecular level, liquid-state NMR spectroscopy and molecular dynamics (MD) simulations were performed.

Liquid-state ^{1}H and ^{13}C single-pulse NMR experiments were performed under quantitative conditions on electrolytes with 0.1 M $Zn(TFSI)_2$ and different [EMIm]TFSI:GBL volume ratios (Figure 4a,b). The ^{1}H single-pulse spectra for the single-solvent electrolytes yielded ^{1}H signals corresponding to either $EMIm^+$ or GBL, as expected (Figure 4a). In the mixed-solvent electrolytes, the $EMIm^+$ and GBL ^{1}H chemical shifts increased as the GBL content increased (i.e., volume ratio of [EMIm]-TFSI:GBL decreased), a result of slightly reduced nuclear shielding in these species due to average changes in intermolecular interactions. As anticipated, the ^{13}C chemical shifts for the single-solvent electrolytes corresponded closely to their expected values (Figure 4b). However, upon mixing, subtle changes in the ^{13}C chemical shifts of the GBL signals reveal insights into the local coordination environments (Figure 4c). In particular, the ^{13}C carbonyl signal of GBL (carbon '1') is strongly affected due to its role in Zn^{2+} cation solvation; interestingly, the changes in shift of this ^{13}C signal mimic the trends of the viscosity curve (Figure 2c), rather than the monotonic change that might be expected. As shown by MD simulations below, this non-monotonic trend arises from a

https://doi.org/10.1021/acs.jpclett.3c00150
J. Phys. Chem. Lett. 2023, 14, 2378−2386

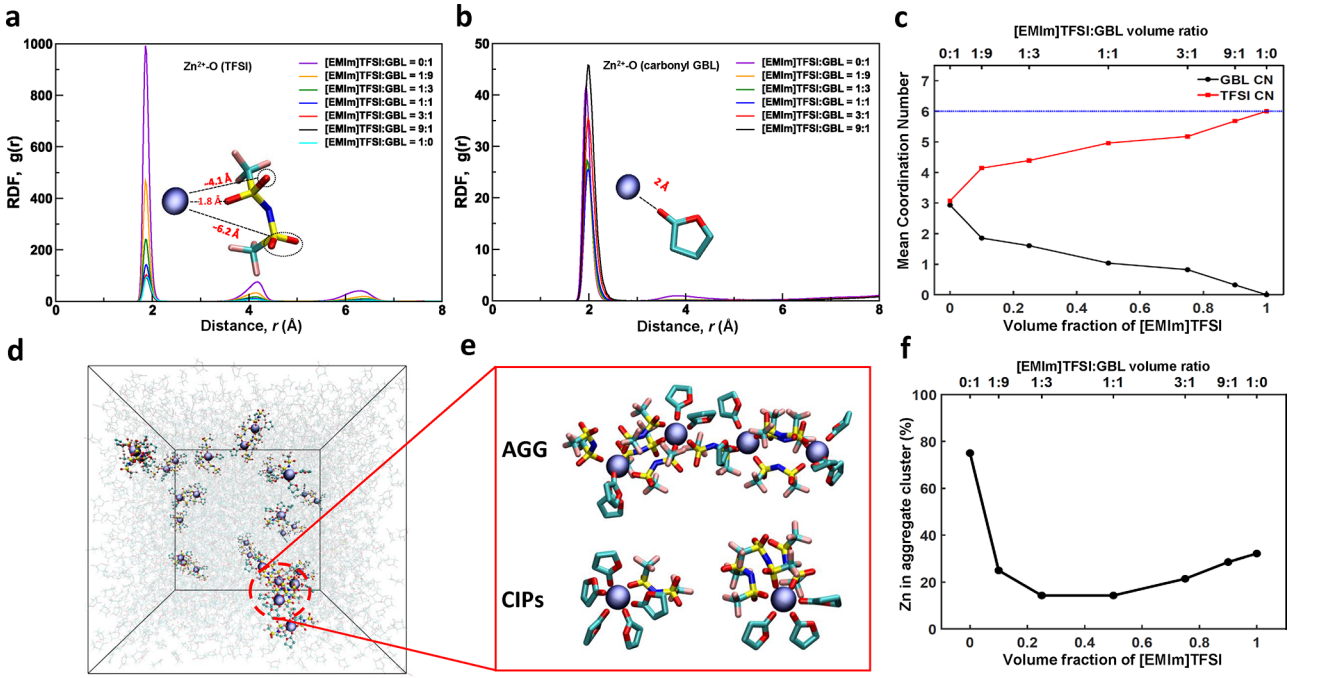

Figure 5. (a) Radial distribution function (RDF) of Zn−O distances between Zn^{2+} cations and $TFSI^-$ oxygen atoms for electrolytes with 0.1 M $Zn(TFSI)_2$ in [EMIm]TFSI:GBL with volume ratios of 0:1, 1:9, 1:3, 1:1, 3:1, 9:1 and 1:0. *Inset*: Schematic of a Zn-TFSI interaction, highlighting Zn−O distances. (b) RDF of Zn−O distances between Zn^{2+} and the GBL carbonyl oxygen atom. *Inset*: Schematic of a Zn-GBL interaction, highlighting the Zn−O (carbonyl) distance. (c) Mean number of GBL and TFSI molecules in the primary Zn solvation sphere. (d) Snapshot of the MD simulation box for the single-solvent electrolyte composed of 0.1 M $Zn(TFSI)_2$ in GBL at 298 K. (e) Representations of ion aggregates (AGG) and Zn-TFSI contact ion pairs (CIPs) in this electrolyte. (f) Percentage of Zn^{2+} cations within ion aggregates for each electrolyte formulation.

combination of competing effects associated with the primary and secondary solvation shells of Zn^{2+} cations, including changes in the GBL and TFSI coordination numbers, Zn-GBL interaction distances, and ion aggregation.

The effect of $Zn(TFSI)_2$ concentration was also investigated by comparing liquid-state ^1H and ^{13}C NMR spectra acquired on electrolytes with 0.1 or 1.0 M $Zn(TFSI)_2$ in [EMIm]-TFSI:GBL with a 1:1 volume ratio (Figure S4), yielding insight into the coordinating ability of GBL. In particular, the ^{13}C chemical shifts associated with GBL change significantly with increasing $Zn(TFSI)_2$ salt concentration. While GBL molecules experience changes in their local electronic environments upon increased zinc salt concentration, as indicated by the changes in ^{13}C chemical shift, $EMIm^+$ cations exhibit negligible change in their ^{13}C chemical shifts, establishing that the measured ^{13}C shift changes are specifically due to interactions of GBL with Zn^{2+} cations. Most strikingly, the GBL ^{13}C carbonyl signal (carbon '1') increased 5.3 ppm, from 179.1 to 184.4 ppm, while a concordant positive shift of 2.6 ppm was observed for carbon '4', indicating reduced electron density and hence decreased nuclear shielding for the oxygen-adjacent carbon atoms in GBL upon coordination with Zn^{2+} cations.

To further elucidate the solvation structure of the Zn^{2+} cations in this electrolyte, MD simulations were conducted on electrolytes with 0.1 M $Zn(TFSI)_2$ and [EMIm]TFSI:GBL with different volume ratios. Changes in the coordination environments of zinc were tracked by computing the radial distribution functions (RDFs) of Zn−O distances between Zn^{2+} cations and either $TFSI^-$ anions (Figure 5a, all oxygen atoms) or GBL molecules (Figure 5b, carbonyl oxygen only) for each electrolyte formulation. An intense RDF peak was observed for the Zn−O (TSFI) pair at an average distance of 1.85 Å, which is in agreement with values reported in the literature.[29] This RDF plot also has two sets of broad, low-intensity peaks, at distances of approximately 4.1 and 6.2 Å, which correspond to the more distant oxygen atoms on the same $TFSI^-$ anion, as indicated by the inset schematic. The RDF peak intensities decreased with increasing TFSI concentration as RDF values are normalized to the bulk number density of $TFSI^-$ anions. Additionally, the higher relative RDF peak intensities at lower concentrations of [EMIm]TFSI indicate that $TFSI^-$ anions preferentially form contact ion pairs with Zn^{2+} cations at these compositions. Interestingly, the peak at 6.2 Å moves to higher values as [EMIm]TFSI is added, likely due to a reduction in ion aggregation and change in average orientation of the $TFSI^-$ anions relative to Zn^{2+}. The computed RDF for the Zn−O (GBL carbonyl) pair yields peaks around 2 Å indicating the presence of GBL in the primary coordination sphere. The Zn^{2+} cations exhibit greater interaction distances with GBL than for TFSI, as Zn^{2+} interacts with $TFSI^-$ anions electrostatically.

The primary solvation environment of the Zn^{2+} cations can be understood by analyzing the average coordination numbers of GBL and TFSI. Their relative quantities within the Zn^{2+} solvation sphere were determined by integrating the RDFs (Figure S5). The total number of solvating species totaled six, indicating octahedral coordination of the zinc (Figure 5c). The TFSI coordination number increases with greater [EMIm]-TFSI content, which is also reflected in the greater average Zn-GBL distance that likely occurs due to steric interactions between GBL and the greater number of molecularly proximate TFSI in the solvation sphere. Interestingly, the average number of $TFSI^-$ coordinated to Zn^{2+} in the single-solvent electrolyte composed of 0.1 M $Zn(TFSI)_2$ in GBL is

https://doi.org/10.1021/acs.jpclett.3c00150
J. Phys. Chem. Lett. 2023, 14, 2378−2386

close to three, despite the TFSI:Zn molar ratio being only 2:1. A snapshot of the MD simulation for this electrolyte (Figure 5d) reveals that this outcome arises due to the existence of ion aggregates, within which a single $TFSI^-$ anion can coordinate to two Zn^{2+} cations (Figure 5e).

The percentage of Zn^{2+} cations within ion aggregates was inspected for each electrolyte formulation (Figure 5f). The highest proportion of aggregated Zn (75%) was present in the single-solvent electrolyte containing GBL. Increasing the volume ratio of [EMIm]TFSI:GBL to 1:9 results in a stark reduction in the percentage of Zn^{2+} in aggregates (24%) and, in turn, an increase in the formation of Zn-TFSI contact ion pairs. A minimum in the quantity of Zn^{2+} within aggregates (12%) was observed for electrolytes with [EMIm]TFSI:GBL in 1:3 and 1:1 volume ratios, followed by a monotonic increase to 30% for the single-solvent electrolyte with [EMIm]TFSI.

MD simulations and liquid-state NMR measurements thus revealed multiple competing effects at the molecular level upon increasing the [EMIm]TFSI content that explain the existence of an optimum composition for reversible Zn electrodeposition at low temperatures. These effects include changes in Zn-TFSI contact ion pairs, the coordination numbers of GBL and TFSI, and the number of ion aggregates formed. Note that the minimized ion aggregation in the electrolyte mixture with [EMIm]TFSI:GBL in a volume ratio of 1:3, determined by MD simulations (Figure 5f), coincides with the only mixture capable of electroplating zinc at −60 °C and 0.01 mA cm^{-2} within the 1 V limit, despite having similar overpotentials compared to other mixtures (e.g., 1:9 or 1:1) at higher temperatures (Figure 1b). Adding [EMIm]TFSI to GBL in modest concentrations reduces ion aggregation significantly; also, Zn-TFSI contact ion pairs are favored at lower [EMIm]TFSI concentrations, the formation of which would be expected to reduce the desolvation energy[30,31] of Zn^{2+} cations prior to electrodeposition due to repulsion of $TSFI^-$ anions from the negatively charged zinc metal electrode. Further increasing the [EMIm]TFSI content beyond a [EMIm]TFSI:GBL volume ratio of 1:3 results in increased ion aggregation, greater numbers of $TFSI^-$ anions coordinated to Zn^{2+} cations, and reduced numbers of Zn-TFSI contact ion pairs, while macroscopically, the specific conductivity and Zn diffusion coefficient decrease while the viscosity increases. The balance of reduced ion aggregation and Zn-TFSI contact-ion pairing is particularly critical to understanding the molecular nature of the optimum concentration of low-temperature Zn electrodeposition, whose favorable electrochemical properties cannot be fully explained only by macroscopic properties and thermodynamic arguments.

Although this study focuses on improving low-temperature performance of reversible Zn electrodeposition, often a wide range of operating temperatures are required in the extreme environments demanded by aerospace and defense applications. At high temperatures, limitations associated with electrolyte conductivity are often minimal due to fast ion transport; however, adverse side reactions often arise at elevated temperatures, which accelerate capacity fade and cell failure. Note that ionic liquids are generally more stable than organic solvents at high temperatures.[11] A future investigation is thus warranted to evaluate the high temperature use of these electrolyte mixtures.

In conclusion, electrolytes composed of $Zn(TFSI)_2$ zinc salt in mixtures of [EMIm]TFSI ionic liquid and GBL organic solvent were used to enable low-temperature Zn electroplating and stripping. The optimized electrolyte mixture consisted of 0.1 M $Zn(TFSI)_2$ in [EMIm]TFSI:GBL with a volume ratio of 1:3, which formed a deep eutectic solvent. This electrolyte composition enabled reversible Zn electrodeposition at temperatures as low as −60 °C and had the greatest specific conductivity, highest Zn diffusivity, and lowest viscosity. Low zinc salt concentration was found to be favorable at low temperatures due to the significant increase in viscosity at higher salt concentrations. Liquid-state ^1H and ^{13}C NMR measurements revealed GBL to be in close molecular proximity to Zn^{2+} cations, playing an instrumental role in ion solvation particularly through its carbonyl group. Molecular dynamics simulations indicate that adding [EMIm]TFSI in modest concentrations to GBL disturbs ion aggregate formation. Zn-TFSI contact ion pairs are favored at lower [EMIm]TFSI concentrations, which would be expected to lead to lower-energy zinc desolvation during electrodeposition at the negatively charged zinc electrode. Further increasing the [EMIm]TFSI content beyond a [EMIm]TFSI:GBL volume ratio of 1:3 increases ion aggregation and reduces Zn-TFSI contact ion pairs. Overall, this work reveals strategies for how to design electrolytes that enable the low-temperature electrodeposition of metal cations while demonstrating an electrolyte mixture with applications for low-temperature Zn metal batteries.

METHODS

Electrolyte preparation. Electrolyte solutions were prepared, and cells were assembled in an argon-filled glovebox with H_2O and O_2 levels below 1 ppm. Electrolyte solutions were prepared at room temperature by mixing 1-ethyl-3-methyl-imidazolium bis(trifluoromethylsulfonyl)imide ([EMIm]TFSI) and γ-butyrolactone (GBL) in [EMIm]TFSI:GBL volume ratios of 1:0, 3:1, 1:1, 1:3, 1:9, and 0:1. Zinc bis(trifluoromethylsulfonyl)-imide ($Zn(TFSI)_2$) was added to 0.1 or 1.0 M (1:1 volume ratio only) concentration based on the neat solvent volumes. The salt and solvents were purchased from Thermo Fisher Scientific without further purification.

Galvanostatic cycling. Zn-Zn symmetric two-electrode cells were assembled using zinc foil (Thermo Fisher Scientific; 99.95% pure). Polytetrafluorethylene (PTFE) Swagelok unions with diameters of 1/4″ (6.35 mm) were used as airtight cell housing. Molybdenum (Mo) rods or were used as current collectors for both electrodes for galvanostatic testing. A glass microfiber filter (GF/D, Whatman) was used as a separator. 50 μL of electrolyte was added to the 1/4″ Swagelok cells. Galvanostatic cycling was performed on an Arbin LBT battery tester. Symmetric Zn-Zn cells were cycled at 0.01 mA cm^{-2} in 45 min half-cycles, which was repeated until the end of a temperature testing period or until cell potential exceeded ±1.0 V to ensure stability of the Mo rods. Variable-temperature electrochemical cycling was performed in an environmental chamber (ESPEC BTZ-133) using the following temperature sequence: 25, 0, −20, −40, −60, 25 °C. Measurements were taken after a 1 h temperature equilibration period. The temperature was held at each step for 10 h while galvanostatic cycling was performed.

Electrochemical measurements. Cyclic voltammetry (CV) and galvanostatic electrochemical impedance spectroscopy (GEIS) measurements were performed in a three-electrode cell using a Biologic VSP-300 potentiostat to determine the diffusion coefficient D of zinc ions, viscosity η, and specific conductivity σ of the electrolyte. The cell contained glassy carbon as the

https://doi.org/10.1021/acs.jpclett.3c00150
J. Phys. Chem. Lett. 2023, 14, 2378−2386

working and counter electrodes (Alfa Aesar; 0.1256 cm^2) and Zn-wire (Thermo Fisher Scientific; 0.5 mm tip radius) as a quasi-reference electrode. CV curves were recorded between 1 and −0.5 V vs. Zn/Zn^{2+} at variable scan rates (3 to 10 mV s^{-1}) to calculate Zn diffusion coefficients and electrolyte viscosities by using the Randles-Ševčík (eq 1) and Stokes-Einstein (eq 2) relationships, respectively:

$$i = 0.4463zFAc_0\left(\frac{zF\nu D}{RT}\right)^{1/2} \quad (1)$$

$$\eta = \frac{k_B T}{6D\pi r} \quad (2)$$

where F is Faraday's constant, R is the universal gas constant, k_B is Boltzmann's constant, c_0 is the bulk concentration of Zn^{2+} ions (0.001 to 0.0001 mol cm^{-3}), A is the electrode surface area (0.1256 cm^2), z is number of transferred electrons ($2e^-$), ν is the scan rate (3 to 10 mV s^{-1}), r is the Zn^{2+} ion radius (70 pm), and T is the temperature (25 °C). GEIS measurements were performed with a 100 μA perturbation signal at 0 mA from 1 Hz to 500 kHz. The specific conductivity was then calculated by the determined inner resistance, R, the inter-electrode distance of 0.5 cm, and electrode area of 0.1256 cm^2.

Differential scanning calorimetry. Differential scanning calorimetry (DSC) measurements were performed using DSC Q200 (TA Instruments). DSC samples were prepared in an argon-filled glovebox with H_2O and O_2 levels below 1 ppm. For each electrolyte sample, 8 μL was placed into an aluminum hermetic pan, weighed, and then sealed with a crimper within the glovebox. The electrolyte samples were subject to the following heat treatment. The sample was cooled initially from room temperature at a rate of 2 °C/min down to −80 °C before holding the temperature at −80 °C for 10 min. The samples were then heated to 40 °C at a rate of 2 or 5 °C/min.

Nuclear magnetic resonance spectroscopy. Samples were prepared inside 3 mm liquid NMR tubes sealed with epoxy and inserted coaxially into 5 mm NMR tubes containing D_2O for the solvent lock to avoid interaction with the electrolyte. Liquid-state ^1H and ^{13}C NMR experiments were performed on a Bruker Avance III HD 600 NMR spectrometer with a 14.1 T superconducting magnet equipped with a Bruker 5 mm Triple Resonance Inverse TXI Probe (600S3 H−P/C−D-05 Z-gradient) operating at 600.13 and 150.90 MHz for ^1H and ^{13}C nuclei, respectively. Liquid-state single-pulse ^1H NMR spectra were acquired under quantitative conditions using 26 or 31 kHz rf field strengths (optimized on sample) as well as recycle delays of 21−30 s (optimized on sample), after which all spins relaxed to thermal equilibrium. Liquid-state single-pulse ^{13}C NMR spectra were acquired using an 18 kHz rf field strength and 30 s recycle delays.

Molecular dynamics simulations. All simulations were performed on GROMACS[32,33] using the OPLS-AA force field.[34] The OPLS parameters for the ionic liquid EMIm-[TFSI] were taken from Doherty et al.,[35] whereas GBL was parametrized using the LigParGen server.[36] The nonbonded interaction parameters for Zn^{2+} cations were obtained from Li et al.[37] An 8 nm cubic box with 28 Zn^{2+} cations, corresponding to a concentration of 0.1 M $Zn(TFSI)_2$, was employed for all simulations. Initial configurations for each composition were generated using PACKMOL.[38] The particle mesh Ewald (PME) algorithm[39,40] was adopted for the electrostatic interactions, and starting velocities were generated using a Maxwell distribution. Following energy minimization with the steepest descent algorithm, each system was pre-equilibrated with canonical ensemble (NVT) and isothermal-isobaric ensemble (NPT) runs (1 ns each) at 298 K. The temperature and pressure of the system were maintained using a modified Berendsen thermostat and Parrinello-Rahman algorithm, respectively.[41] The final runs were then performed for 500 ns at 298 K with a 2 fs integration step. Simulation trajectories and zinc solvation structures were visualized using the VMD software.[42]

■ ASSOCIATED CONTENT

Supporting Information

The Supporting Information is available free of charge at https://pubs.acs.org/doi/10.1021/acs.jpclett.3c00150.

DSC measurements, liquid-state ^1H and ^{13}C NMR measurements, and MD simulation results (PDF)

■ AUTHOR INFORMATION

Corresponding Author

Robert J. Messinger − *Department of Chemical Engineering, The City College of New York, New York, New York 10031, United States;* orcid.org/0000-0002-5537-3870; Email: rmessinger@ccny.cuny.edu

Authors

Brendan E. Hawkins − *Department of Chemical Engineering, The City College of New York, New York, New York 10031, United States;* orcid.org/0000-0001-6238-4239

Theresa Schoetz − *Department of Chemical Engineering, The City College of New York, New York, New York 10031, United States*

Leo W. Gordon − *Department of Chemical Engineering, The City College of New York, New York, New York 10031, United States;* orcid.org/0000-0002-8242-9470

Surabh KT − *Department of Chemical Engineering, The City College of New York, New York, New York 10031, United States*

Jonah Wang − *Department of Chemical Engineering, The City College of New York, New York, New York 10031, United States*

Complete contact information is available at: https://pubs.acs.org/10.1021/acs.jpclett.3c00150

Notes

The authors declare no competing financial interest.

■ ACKNOWLEDGMENTS

The authors gratefully acknowledge support from the U.S. National Aeronautics and Space Administration (NASA) via the NASA-CCNY Center for Advanced Batteries for Space under cooperative agreement 80NSSC19M0199 and the U.S. National Science Foundation (NSF) under CAREER award CBET-1847552. NMR measurements were performed at the City University of New York (CUNY) Advanced Science Research Center. MD simulations were performed at the CUNY High Performance Computing Center at the College of Staten Island, which is supported in part by NSF Awards CNS-0958379, CNS-0855217, ACI-1126113, and OEC-2215760.

REFERENCES

(1) Brandon, E. J.; West, W. C.; Smart, M. C.; Whitcanack, L. D.; Plett, G. A. Extending the low temperature operational limit of double-layer capacitors. *J. Power Sources* **2007**, *170* (1), 225−232.

(2) Smart, M. C.; Ratnakumar, B. V.; Surampudi, S. Electrolytes for low-temperature lithium batteries based on ternary mixtures of aliphatic carbonates. *J. Electrochem. Soc.* **1999**, *146* (2), 486.

(3) Xu, K. Nonaqueous liquid electrolytes for lithium-based rechargeable batteries. *Chem. Rev.* **2004**, *104* (10), 4303−4418.

(4) Jones, J.-P.; Smart, M. C.; Krause, F. C.; West, W. C.; Brandon, E. J. Batteries for robotic spacecraft. *Joule* **2022**, *6* (5), 923−928.

(5) Jaguemont, J.; Boulon, L.; Dubé, Y. A comprehensive review of lithium-ion batteries used in hybrid and electric vehicles at cold temperatures. *Appl. Energy* **2016**, *164*, 99−114.

(6) Gupta, A.; Manthiram, A. Designing advanced lithium-based batteries for low-temperature Conditions. *Adv. Energy Mater.* **2020**, *10* (38), 2001972.

(7) Marsh, R. A.; Vukson, S.; Surampudi, S.; Ratnakumar, B. V.; Smart, M. C.; Manzo, M.; Dalton, P. J. Li ion batteries for aerospace applications. *J. Power Sources* **2001**, *97*, 25−27.

(8) Smith, E. L.; Abbott, A. P.; Ryder, K. S. Deep eutectic solvents (DESs) and their applications. *Chem. Rev.* **2014**, *114* (21), 11060−11082.

(9) Wu, J.; Liang, Q.; Yu, X.; Lu, Q.-F.; Ma, L.; Qin, X.; Chen, G.; Li, B. Deep eutectic solvents for boosting electrochemical energy storage and conversion: a review and perspective. *Adv. Funct. Mater.* **2021**, *31* (22), 2011102.

(10) Xu, Y.; Lin, W. J.; Gliege, M.; Gunckel, R.; Zhao, Z.; Yu, H.; Dai, L. L. A Dual Ionic Liquid-Based Low-Temperature Electrolyte System. *J. Phys. Chem. B* **2018**, *122* (50), 12077−12086.

(11) Giffin, G. A. Ionic liquid-based electrolytes for "beyond lithium" battery technologies. *J. Mater. Chem. A* **2016**, *4* (35), 13378−13389.

(12) Liu, Z.; Luo, X.; Qin, L.; Fang, G.; Liang, S. Progress and prospect of low-temperature zinc metal batteries. *Adv. Powder Mater.* **2022**, *1* (2), 100011.

(13) Liu, S.; Zhang, R.; Mao, J.; Zhao, Y.; Cai, Q.; Guo, Z. From room temperature to harsh temperature applications: Fundamentals and perspectives on electrolytes in zinc metal batteries. *Sci. Adv.* **2022**, *8* (12), eabn5097.

(14) Hawkins, B. E.; Turney, D. E.; Messinger, R. J.; Kiss, A. M.; Yadav, G. G.; Banerjee, S.; Lambert, T. N. Electroactive ZnO: Mechanisms, Conductivity, and Advances in Zn Alkaline Battery Cycling. *Adv. Energy Mater.* **2022**, *12* (15), 2103294.

(15) Parker, J. F.; Chervin, C. N.; Pala, I. R.; Machler, M.; Burz, M. F.; Long, J. W.; Rolison, D. R. Rechargeable nickel−3D zinc batteries: An energy-dense, safer alternative to lithium-ion. *Science* **2017**, *356* (6336), 415−418.

(16) Service, R. F. Zinc aims to beat lithium batteries at storing energy. *Science* **2021**, *372* (6545), 890−891.

(17) Ma, L.; Chen, S.; Li, N.; Liu, Z.; Tang, Z.; Zapien, J. A.; Chen, S.; Fan, J.; Zhi, C. Hydrogen-free and dendrite-free all-solid-state Zn-ion batteries. *Adv. Mater.* **2020**, *32* (14), 1908121.

(18) Qiu, H.; Du, X.; Zhao, J.; Wang, Y.; Ju, J.; Chen, Z.; Hu, Z.; Yan, D.; Zhou, X.; Cui, G. Zinc anode-compatible in-situ solid electrolyte interphase via cation solvation modulation. *Nat. Commun.* **2019**, *10* (1), 5374.

(19) Chang, N.; Li, T.; Li, R.; Wang, S.; Yin, Y.; Zhang, H.; Li, X. An aqueous hybrid electrolyte for low-temperature zinc-based energy storage devices. *Energy Environ. Sci.* **2020**, *13* (10), 3527−3535.

(20) Monti, D.; Jónsson, E.; Palacín, M. R.; Johansson, P. Ionic liquid based electrolytes for sodium-ion batteries: Na^+ solvation and ionic conductivity. *J. Power Sources* **2014**, *245*, 630−636.

(21) Simons, T. J.; Howlett, P. C.; Torriero, A. A. J.; MacFarlane, D. R.; Forsyth, M. Electrochemical, transport, and spectroscopic properties of 1-ethyl-3-methylimidazolium ionic liquid electrolytes containing zinc dicyanamide. *J. Phys. Chem. C* **2013**, *117* (6), 2662−2669.

(22) Tian, J.; Cui, C.; Xie, Q.; Qian, W.; Xue, C.; Miao, Y.; Jin, Y.; Zhang, G.; Guo, B. EMIMBF 4−GBL binary electrolyte working at−70° C and 3.7 V for a high performance graphene-based capacitor. *J. Mater. Chem. A* **2018**, *6* (8), 3593−3601.

(23) Wen, X.; Liu, Y.; Xu, D.; Zhao, Y.; Lake, R. K.; Guo, J. Room-Temperature Electrodeposition of Aluminum via Manipulating Coordination Structure in $AlCl_3$ Solutions. *J. Phys. Chem. Lett.* **2020**, *11* (4), 1589−1593.

(24) Hansen, B. B.; Spittle, S.; Chen, B.; Poe, D.; Zhang, Y.; Klein, J. M.; Horton, A.; Adhikari, L.; Zelovich, T.; Doherty, B. W.; Gurkan, B.; et al. Deep eutectic solvents: A review of fundamentals and applications. *Chem. Rev.* **2021**, *121* (3), 1232−1285.

(25) Zhang, W.; Xia, H.; Zhu, Z.; Lv, Z.; Cao, S.; Wei, J.; Luo, Y.; Xiao, Y.; Liu, L.; Chen, X. Decimal solvent-based high-entropy electrolyte enabling the extended survival temperature of lithium-ion batteries to −130° C. *CCS Chemistry* **2021**, *3* (4), 1245−1255.

(26) Yalkowsky, S. H. Carnelley's Rule and the Prediction of Melting Point. *J. Pharm. Sci.* **2014**, *103* (9), 2629−2634.

(27) Kirchner, B.; Malberg, F.; Firaha, D. S; Holloczki, O. Ion pairing in ionic liquids. *Journal of Physics: Condens. Matter* **2015**, *27* (46), 463002.

(28) Dong, K.; Liu, X.; Dong, H.; Zhang, X.; Zhang, S. Multiscale studies on ionic liquids. *Chem. Rev.* **2017**, *117* (10), 6636−6695.

(29) Busato, M.; D'Angelo, P.; Melchior, A. Solvation of Zn^{2+} ion in 1-alkyl-3-methylimidazolium bis (trifluoromethylsulfonyl) imide ionic liquids: a molecular dynamics and X-ray absorption study. *Phys. Chem. Chem. Phys.* **2019**, *21* (13), 6958−6969.

(30) Holoubek, J.; Liu, H.; Wu, Z.; Yin, Y.; Xing, X.; Cai, G.; Yu, S.; Zhou, H.; Pascal, T. A.; Chen, Z.; Liu, P. Tailoring electrolyte solvation for Li metal batteries cycled at ultra-low temperature. *Nat. Energy* **2021**, *6* (3), 303−313.

(31) Holoubek, J.; Baskin, A.; Lawson, J. W.; Khemchandani, H.; Pascal, T. A.; Liu, P.; Chen, Z. Predicting the Ion Desolvation Pathway of Lithium Electrolytes and Their Dependence on Chemistry and Temperature. *J. Phys. Chem. Lett.* **2022**, *13* (20), 4426−4433.

(32) Pronk, S.; Páll, S.; Schulz, R.; Larsson, P.; Bjelkmar, P.; Apostolov, R.; Shirts, M. R.; Smith, J. C.; Kasson, P. M.; van der Spoel, D.; Hess, B.; Lindahl, E. GROMACS 4.5: A High-Throughput and Highly Parallel Open Source Molecular Simulation Toolkit. *Bioinformatics* **2013**, *29* (7), 845−854.

(33) Abraham, M. J.; Murtola, T.; Schulz, R.; Páll, S.; Smith, J. C.; Hess, B.; Lindahl, E. GROMACS: High Performance Molecular Simulations through Multi-Level Parallelism from Laptops to Supercomputers. *SoftX* **2015**, *1*, 19−25.

(34) Jorgensen, W. L.; Maxwell, D. S.; Tirado-Rives, J. Development and Testing of the OPLS All-Atom Force Field on Conformational Energetics and Properties of Organic Liquids. *J. Am. Chem. Soc.* **1996**, *118* (45), 11225−11236.

(35) Doherty, B.; Zhong, X.; Gathiaka, S.; Li, B.; Acevedo, O. Revisiting OPLS Force Field Parameters for Ionic Liquid Simulations. *J. Chem. Theory Comput.* **2017**, *13* (12), 6131−6135.

(36) Dodda, L. S.; Cabeza de Vaca, I.; Tirado-Rives, J.; Jorgensen, W. L. LigParGen Web Server: An Automatic OPLS-AA Parameter Generator for Organic Ligands. *Nucleic Acids Res.* **2017**, *45* (W1), W331−W336.

(37) Li, P.; Roberts, B. P.; Chakravorty, D. K.; Merz, K. M. Rational Design of Particle Mesh Ewald Compatible Lennard-Jones Parameters for + 2 Metal Cations in Explicit Solvent. *J. Chem. Theory Comput.* **2013**, *9* (6), 2733−2748.

(38) Martinez, L.; Andrade, R.; Birgin, E. G.; Martínez, J. M. PACKMOL: A Package for Building Initial Configurations for Molecular Dynamics Simulations. *J. Comput. Chem.* **2009**, *30* (13), 2157−2164.

(39) Darden, T.; York, D.; Pedersen, L. Particle Mesh Ewald: An N·log(N) Method for Ewald Sums in Large Systems. *J. Chem. Phys.* **1993**, *98* (12), 10089.

(40) Essmann, U.; Perera, L.; Berkowitz, M. L.; Darden, T.; Lee, H.; Pedersen, L. G. A Smooth Particle Mesh Ewald Method. *J. Chem. Phys.* **1995**, *103* (19), 8577.

https://doi.org/10.1021/acs.jpclett.3c00150
J. Phys. Chem. Lett. 2023, 14, 2378−2386

(41) Parrinello, M.; Rahman, A. Polymorphic Transitions in Single Crystals: A New Molecular Dynamics Method. *J. Appl. Phys.* **1981**, *52* (12), 7182.
(42) Humphrey, W.; Dalke, A.; Schulten, K. VMD: Visual Molecular Dynamics. *J. Mol. Graph.* **1996**, *14* (1), 33−38.

https://doi.org/10.1021/acs.jpclett.3c00150
J. Phys. Chem. Lett. 2023, 14, 2378−2386